2011

Construction of low dissipative high-order well-balanced filter schemes for non-equilibrium flows

Wei Wang
Stanford University

Helen C. Yee
yee@nas.nasa.gov

Bjorn Sjögreen
Lawrence Livermore National Laboratories, sjogreen2@llnl.gov

Thierry Magin
Stanford University

Chi-Wang Shu
Brown University, shu@dam.brown.edu

Journal of Computational Physics 230 (2011) 4316–4335

Contents lists available at ScienceDirect

Journal of Computational Physics

journal homepage: www.elsevier.com/locate/jcp

Construction of low dissipative high-order well-balanced filter schemes for non-equilibrium flows

Wei Wang [a], H.C. Yee [b], Björn Sjögreen [c], Thierry Magin [a], Chi-Wang Shu [d,*]

[a] Center for Turbulence Research, Stanford University, Stanford, CA 94305, United States
[b] NASA Ames Research Center, Moffett Field, CA 94035, United States
[c] Lawrence Livermore National Laboratory, Livermore, CA 94551, United States
[d] Division of Applied Mathematics, Brown University, Providence, RI 02912, United States

ARTICLE INFO

Article history:
Available online 29 April 2010

Keywords:
High-order filter methods
WENO schemes
Well-balanced schemes
Non-equilibrium flow
Chemical reactions
1D turbulence/shock interactions

ABSTRACT

The goal of this paper is to generalize the well-balanced approach for non-equilibrium flow studied by Wang et al. (2009) [29] to a class of low dissipative high-order shock-capturing filter schemes and to explore more advantages of well-balanced schemes in reacting flows. More general 1D and 2D reacting flow models and new examples of shock turbulence interactions are provided to demonstrate the advantage of well-balanced schemes. The class of filter schemes developed by Yee et al. (1999) [33], Sjögreen and Yee (2004) [27] and Yee and Sjögreen (2007) [38] consist of two steps, a full time step of spatially high-order non-dissipative base scheme and an adaptive non-linear filter containing shock-capturing dissipation. A good property of the filter scheme is that the base scheme and the filter are stand-alone modules in designing. Therefore, the idea of designing a well-balanced filter scheme is straightforward, i.e. choosing a well-balanced base scheme with a well-balanced filter (both with high-order accuracy). A typical class of these schemes shown in this paper is the high-order central difference schemes/predictor–corrector (PC) schemes with a high-order well-balanced WENO filter. The new filter scheme with the well-balanced property will gather the features of both filter methods and well-balanced properties: it can preserve certain steady-state solutions exactly; it is able to capture small perturbations, e.g. turbulence fluctuations; and it adaptively controls numerical dissipation. Thus it shows high accuracy, efficiency and stability in shock/turbulence interactions. Numerical examples containing 1D and 2D smooth problems, 1D stationary contact discontinuity problem and 1D turbulence/shock interactions are included to verify the improved accuracy, in addition to the well-balanced behavior.

1. Introduction

Recent progress in the development of a class of low dissipative high-order filter schemes for multiscale Navier–Stokes and magnetohydrodynamics (MHD) systems [33,39,27,35,26,36–38] shows good performance in multiscale shock/turbulence simulations.

The highly parallelizable high-order filter methods consist of two steps, a full time step of spatially high-order non-dissipative (or very low dissipative) base scheme and an adaptive multistep filter. The non-linear filter consists of the product of a wavelet-based flow sensor and the dissipative portion of a high-order shock-capturing scheme. The

* Corresponding author. Tel.: +1 401 863 2549; fax: +1 401 863 1355.
E-mail address: shu@dam.brown.edu (C.-W. Shu).

0021-9991/$ - see front matter © 2010 Elsevier Inc. All rights reserved.
doi:10.1016/j.jcp.2010.04.033

built-in flow sensors in the post processing filter control the amounts and types of numerical dissipation. The filter switches on the dissipations only where needed, and leaves the rest of the flow region free from numerical dissipation. Only the filter step might involve the use of flux limiters and approximate Riemann solvers as stabilizing mechanisms to remove Gibbs phenomena related spurious oscillations resulting from the base scheme step. The more scales that are resolved by the base scheme, the less the filter is utilized, thereby gaining accuracy and computational time as the grid is refined. The adaptive numerical dissipation control idea is very general and can be used in conjunction with spectral, spectral element, finite element, discontinuous Galerkin, finite volume, and finite difference spatial base schemes. The type of shock-capturing schemes used as non-linear dissipation can be the dissipative portion of any high-resolution TVD, MUSCL, ENO, or WENO shock-capturing method [33,13,23]. By design, flow sensors, spatial base schemes and linear and non-linear dissipation models are stand-alone modules. Therefore, a whole class of low dissipative high-order schemes can be derived at ease.

In a recent paper by Wang et al. [29], well-balanced finite difference WENO schemes and second-order TVD schemes were studied for chemical non-equilibrium flows, extending the well-balanced finite difference WENO schemes for shallow water equations in [30,31]. A well-balanced scheme [7,15,5], which can preserve certain non-trivial steady-state solutions exactly, may help minimize some of the spurious oscillations around steady states. It was also shown in [29] that the well-balanced schemes capture small perturbations of the steady-state solutions with high accuracy. While general schemes can only resolve perturbations at the level of truncation error with the specific grid, well-balanced schemes can resolve much smaller perturbations, usually of size 1% or lower of the main steady-state flow.

In this paper the same approach will be applied to construct a high-order well-balanced filter scheme for one temperature non-equilibrium flow with reaction terms. The multi-dimensional hyperbolic system of conservation laws with source terms (also called a balance law)

$$U_t + \nabla \cdot F(U) = S(U) \tag{1}$$

is considered, where U is the solution vector, $F(U)$ is the convective flux and $S(U)$ is the source term. For this type of flow the space variable $\mathbf{x}$ does not appear explicitly in the source term. Thus, the construction of well-balanced schemes can easily go from one-dimension to multi-dimensions. In this paper, comparing with our earlier work [29], more general 1D and 2D reacting flow models and new examples of shock turbulence interactions are provided to demonstrate the advantage of well-balanced schemes.

The designing of well-balanced filter schemes is to choose a well-balanced base scheme and a well-balanced filter part. Then, the filter scheme is almost well-balanced everywhere except at the interfaces of the filtered region and the non-filtered region (see Section 4). Note that in this paper, a 'well-balanced filter scheme' refers to such almost well-balancedness. For the filter scheme without the flow sensor, the resulting filter scheme is well-balanced.

The choice of the sensor will not destroy the well-balanced properties. It has been shown in the previous work [29] that linear schemes, the second-order Predictor–Corrector (PC) scheme [34,16] with TVD filters (such as the Harten–Yee TVD filter [32,33]), and WENO-Roe schemes are well-balanced for certain steady-state solutions with zero velocity. A well-balanced WENO-LF scheme has also been constructed for this type of steady-state solutions. High-order PC schemes are linear schemes and thus well-balanced. Therefore, the new filter schemes presented in this paper, CENTVDfi/CENWENOfi or PCTVDfi/PCWENOfi which utilize central (CEN)/PC schemes as base schemes and the Harten–Yee TVD filter (TVDfi) or the well-balanced WENO schemes as filter (WENOfi) will be well-balanced. We remark that this paper is confined mainly to the spatial discretizations. Appropriate time discretizations should be an integral part of the algorithm.

In this paper, only the zero-velocity steady state of the reacting flow equations will be considered in the numerical tests. A steady state with zero velocity implies that the flow has constant pressure and is in chemical equilibrium. It will be shown that, similarly to well-balanced WENO schemes, well-balanced filter schemes give machine round-off errors regardless of the mesh sizes for the steady-state solutions of the reactive flow equations. Consequently, they can resolve small perturbations of such steady-state solutions well, even with very coarse meshes.

Since the regular high-order low dissipative filter schemes are designed for shock/turbulence interactions and the well-balanced schemes can capture small perturbations of the steady-state solutions with high accuracy, the new well-balanced filter schemes take the advantages of both, thereby making them well suited for computations of turbulent fluctuations on a mainly steady flow field.

The outline of the paper is as follows: in Section 2, the governing equations and the physical model are described. High-order filter schemes are reviewed in Section 3. A brief description of well-balanced schemes and the construction of high-order well-balanced filter scheme are given in Section 4. Numerical examples will be shown in Section 5. Finally, Section 6 gives conclusions and plans for future work. A brief description of high-order PC schemes and the considered time discretization are presented in the Appendix.

2. Governing equations and the physical model

Considering a flow in chemical non-equilibrium and thermal equilibrium, the thermodynamic properties account for excitation of the electronic states for the atoms and molecules, and rovibrational states based on the rigid-rotor harmonic-oscillator approximation for molecules [17,20].

Assuming neither dissipative effects nor radiation, the considered physical model is a system of hyperbolic conservation laws with source terms denoted by

$$U_t + \nabla \cdot F(U) = S(U), \tag{2}$$

$$U = \begin{pmatrix} \rho_1 \\ \cdots \\ \rho_{n_s} \\ \rho \mathbf{u} \\ \rho e \end{pmatrix}; \quad F(U) = \begin{pmatrix} \rho_1 \mathbf{u} \\ \cdots \\ \rho_{n_s} \mathbf{u} \\ \rho \mathbf{u}\mathbf{u}^T + pI \\ (\rho e + p)\mathbf{u} \end{pmatrix}; \quad S(U) = \begin{pmatrix} b_1 \\ \cdots \\ b_{n_s} \\ 0 \\ 0 \end{pmatrix}; \tag{3}$$

where n_s is the number of species, ρ_s, the mass density of species s, $\mathbf{u}$, the velocity vector, and e, the internal energy per unit mass of the mixture. The mixture mass density is defined as $\rho = \sum_{s=1}^{n_s} \rho_s$, and the pressure p is given by the perfect gas law

$$p = RT \sum_{s=1}^{n_s} \frac{\rho_s}{M_s}, \tag{4}$$

where R is the universal gas constant, and M_s, the molar mass of species s. The temperature T can be found from a given total energy by solving

$$\rho e = \sum_{s=1}^{n_s} \rho_s e_s(T) + \frac{1}{2}\rho |\mathbf{u}|^2, \tag{5}$$

for T. The internal energy e_s of species s is a function of temperature

$$e_s(T) = e_s^T(T) + e_s^E(T) + e_s^F, \quad s \in H_a, \tag{6}$$

$$e_s(T) = e_s^T(T) + e_s^E(T) + e_s^R(T) + e_s^V(T) + e_s^F, \quad s \in H_p, \tag{7}$$

where H_a is the set of atoms and H_p is the set of molecules. The superscripts "T" denotes translation, "E" denotes electronic, "R" denotes rotation, "V" denotes vibration and "F" denotes formation. The translational energy of species s is given by

$$e_s^T(T) = \frac{3}{2}\frac{R}{M_s}T, \tag{8}$$

and the electronic energy contribution by

$$e_s^E(T) = \frac{R}{M_s} \frac{\sum_n g_{s,n}^E \theta_{s,n}^E \exp\left(\frac{-\theta_{s,n}^E}{T}\right)}{\sum_n g_{s,n}^E \exp\left(\frac{-\theta_{s,n}^E}{T}\right)}, \tag{9}$$

where quantities $g_{s,n}^E$ and $\theta_{s,n}^E$ stand for the degeneracy and characteristic temperature of the electronic level n of species s. Only a finite number of electronic states is retained in the computation of partition function. The maximum number of electronic levels of each atom and molecule is progressively increased up to a correspondence between the values of computed enthalpies and accurate reference tables. For molecule s, the rotational energy is assumed to be described by means of a rigid rotor model

$$e_s^R(T) = \frac{RT}{M_s}, \tag{10}$$

and the vibrational energy, by means of a harmonic oscillator model

$$e_s^V(T) = \frac{R}{M_s} \frac{\theta_s^V}{\exp\left(\frac{\theta_s^V}{T}\right) - 1}, \tag{11}$$

where the quantity θ_s^V stands for the vibrational characteristic temperature of the diatomic molecule. To account for the energy released in the gas by chemical reactions between the species, a common level from which all the energies are measured is established by using the formation enthalpy e_s^F at 0 °K.

Consider J reactions of the form

$$\nu'_{1,j} X_1 + \nu'_{2,j} X_2 + \cdots + \nu'_{n_s,j} X_{n_s} \rightleftharpoons \nu''_{1,j} X_1 + \nu''_{2,j} X_2 + \cdots + \nu''_{n_s,j} X_{n_s}, \quad j = 1, \ldots, J, \tag{12}$$

where $\nu'_{i,j}$ and $\nu''_{i,j}$ are respectively the stoichiometric coefficients for the reactants and products of species i in the jth reaction. The ith component b_i of the source term $S(U)$ describes the rate of production of species i due to chemical reaction

$$b_i = M_i \sum_{j=1}^{J} (\nu''_{ij} - \nu'_{ij}) \left[k_{fj} \prod_{s=1}^{n_s} \left(\frac{\rho_s}{M_s}\right)^{\nu'_{s,j}} - k_{bj} \prod_{s=1}^{n_s} \left(\frac{\rho_s}{M_s}\right)^{\nu''_{s,j}} \right], \quad i = 1, \ldots, n_s, \tag{13}$$

where $k_{f,j}(T)$ and $k_{b,j}(T)$ are the forward and backward reaction rate coefficients which are functions of temperature. The forward reaction rate coefficient is given by an Arrhenius law. Following microreversibility the backward rate coefficient is obtained from the expression $k_{f,j} = k_{b,j}/K_{e,j}$, where the equilibrium constant for the jth reaction is given by the relation

$$\ln K_{e,j} = -\frac{1}{k_{BT}} \sum_{s=1}^{n_s} [(\nu'_{s,j} - \nu'_{s,j}) m_s g_s(p_{ref}, T)], \tag{14}$$

where the reference pressure $p_{ref} = 1$ Pa. The Gibbs free energy g_s of species s is a function of pressure and temperature,

$$g_s(p,T) = g_s^T(p,T) + g_s^E(T), \quad s \in H_a, \tag{15}$$
$$g_s(p,T) = g_s^T(p,T) + g_s^E(T) + g_s^R(T) + g_s^V(T), \quad s \in H_p. \tag{16}$$

The translational Gibbs free energy is obtained from

$$g_s^T(p,T) = \frac{RT}{M_s} \ln \left[\frac{RT}{N_A p} \left(\frac{2\pi M_s RT}{N_A^2 h_P^2} \right)^{\frac{3}{2}} \right], \tag{17}$$

where the symbol h_P stands for Planck's constant, and N_A for Avogadro's number. The electronic Gibbs free energy reads

$$g_s^E(T) = -\frac{RT}{M_s} \ln \left[\sum_n g_{s,n}^E \exp \left(\frac{-\theta_{s,n}^E}{T} \right) \right]. \tag{18}$$

For the diatomic molecule s, the rotational Gibbs free energy is

$$g_s^R(T) = -\frac{RT}{M_s} \ln \left(\frac{T}{\theta_s^R \sigma_s} \right), \tag{19}$$

where symbol σ_s stands for the steric factor. The vibrational Gibbs free energy is obtained from the relation

$$g_s^V(T) = \frac{RT}{M_s} \ln \left[1 - \exp \left(\frac{-\theta_s^V}{T} \right) \right]. \tag{20}$$

3. Description of high-order filter methods

For simplicity of presentation, the numerical methods will be described for the one-dimensional equations. In one space dimension F in Eq. (3) becomes a vector. Denote $A = \partial F/\partial U$, the Jacobian matrix of the one-dimensional flux. The eigenvalues of A are

$$(a^1, \ldots, a^m) = (u, \ldots, u, u + c, u - c), \tag{21}$$

where m is the number of components of vector U, $m = n_s + 2$ in the 1D case. c is the frozen speed of sound defined by the expression $c^2 = (\kappa + 1)p/\rho$ with $\kappa = \left(\sum_{s=1}^{n_s} \rho_s R/M_s\right) / \left(\sum_{s=1}^{n_s} \rho_s c_{v,s}\right)$ based on the species specific heat $c_{v,s} = de_s/dT$.

The one dimensional problem is discretized by a uniform grid spacing Δx and the grid points $x_j = j\Delta x$. The time step is denoted by Δt and time levels are $t_n = n\Delta t$. Let U_j^n denote the numerical approximation of $U(x_j, t_n)$. For clarity of presentation, the n- or j-dependencies are left out when they are unimportant in the discussion below.

Let $a_{j+1/2}^l$, and $R_{j+1/2}$ denote the eigenvalues a^l and the eigenvectors R evaluated at some symmetric average of U_j and U_{j+1}, such as Roe's average [24]. Denote R as the matrix whose columns are eigenvectors of A (not to be confused with the R in Eq. (4)). Define

$$\alpha_{j+1/2} = R_{j+1/2}^{-1} (U_{j+1} - U_j) \tag{22}$$

as the difference of the local characteristic variables in the x direction.

The low dissipative high-order filter scheme developed by Yee et al. [33] suggests using the artificial compression method of Harten [9] as a flow sensor to limit the amount of numerical dissipation that is inherent in a scheme. Subsequently, Sjögreen and Yee [27], Yee and Sjögreen [36,38] introduced a wavelet decomposition of the data to determine the location where numerical dissipation is needed. The considered filter method contains two steps, a high-order low dissipative spatial base scheme step (not involving the use of approximate Riemann solvers or flux limiters) and a multistep filter (usually involving the use of approximate Riemann solvers and flux limiters). The non-linear filter consists of the product of a wavelet sensor [27] and the non-linear dissipative portion of a high-resolution shock-capturing scheme.

We will briefly review the high-order filter schemes in this section. For more details, we refer the readers to [33,27,36,38].

3.1. High-order spatial scheme step

The first step of the numerical method consists of a time step via a high-order non-dissipative spatial and temporal base scheme operator L. After the completion of a full time step of the base scheme, the solution is denoted by U^*

$$U^* = L(U^n), \tag{23}$$

where U^n is the numerical solution vector at time level n.

The high-order non-dissipative spatial base scheme could be a standard central scheme, a central compact scheme, or a predictor–corrector (PC) scheme [34,16]. The temporal discretization could be a TVD Runge–Kutta method.

For strong shock interactions and/or steep gradient flows, a small amount of high-order linear dissipation can be added to the base scheme to reduce the time step constraint and stability. For example, an eighth-order linear dissipation with the sixth-order central scheme to approximate $F(U)_x$ is written as

$$\frac{\partial F}{\partial x}|_{x=x_j} \approx D_{06}F_j + d(\Delta x)^7(D_+D_-)^4U_j, \tag{24}$$

where D_{06} is the standard sixth-order accurate centered difference operator, and D_+D_- is the standard second-order accurate centered approximation of the second derivative. The small parameter d is scaled with, e.g. spectral radius of $A(U)$, and is in the range of 0.00001–0.001, depending on the flow problem. d has the sign which gives dissipation in the forward time direction.

In Section 5, we will use high-order central schemes and PC schemes for the base scheme step. Details on these methods, and other choices of spatial base schemes, are given in Appendix A.

3.2. Adaptive non-linear filter step (discontinuities and high gradient capturing)

After the completion of a full time step of the high-order base scheme, the second step is to adaptively filter the solution by the product of a wavelet sensor and the non-linear dissipative portion of a high-resolution shock-capturing scheme (involving the use of flux limiters). The non-linear filter step can be written

$$U_j^{n+1} = U_j^* - \frac{\Delta t}{\Delta x}[H^*_{j+1/2} - H^*_{j-1/2}]. \tag{25}$$

Here, the filter numerical fluxes are defined in the eigenvector basis by $\overline{H}_{j+1/2}$, so that

$$H^*_{j+1/2} = R_{j+1/2}\overline{H}_{j+1/2}. \tag{26}$$

Denote the elements of the vector $\overline{H}_{j+1/2}$ by $\bar{h}^l_{j+1/2}$, $l = 1, 2, \ldots, m$. The non-linear portion of the filter $\bar{h}^l_{j+1/2}$ has the form

$$\bar{h}^l_{j+1/2} = (s^N)^l_{j+1/2}(\phi^l_{j+1/2}). \tag{27}$$

Here, $(s^N)^l_{j+1/2}$ is the sensor to activate the higher-order non-linear numerical dissipation $\phi^l_{j+1/2}$.

The non-linear filter $\phi^l_{j+1/2} = g^l_{j+1/2} - q^l_{j+1/2}$ is the dissipative portion of a high-order high-resolution shock-capturing scheme for the local lth characteristic wave. Here $g^l_{j+1/2}$ and $q^l_{j+1/2}$ are numerical fluxes of the uniformly high-order high-resolution scheme and a high-order central scheme for the lth characteristic wave, respectively.

For the numerical examples, two forms of non-linear dissipation $\phi^l_{j+1/2}$ will be considered, namely:

- Dissipative portion of balanced WENO schemes. It is obtained by taking the full WENO scheme and subtracting the central scheme, such as, WENO5-D_{06} and WENO7-D_{08}.
- Dissipative portion of the Harten–Yee TVD scheme [32,33].

Remark 1. In [38], Yee and Sjögreen proposed and studied both linear and non-linear filters, where the linear filters refer to the standard spectral filter, compact filter, and non-compact high-order linear numerical dissipation. In the present paper, only non-linear filters, especially the dissipative portion of WENO and TVD schemes are considered.

Remark 2. Yee and Sjögreen also did comparisons of applying the filters between "after each Runge–Kutta stage" and "after a full time step". Their research indicated that there is no advantage of applying the filters "after each Runge–Kutta stage". In addition, "after a full time step" is extremely efficient since only one Riemann solve per time step per dimension is required.

3.3. Flow sensor by multiresolution wavelet analysis of the computed flow data

A general description of how to obtain different flow sensors (e.g. $(s^N)^l_{j+1/2}$) by multiresolution wavelet analysis of the computed flow data can be found in Sjögreen and Yee [27] and Yee and Sjögreen [35].

The wavelet flow sensor estimates the Lipschitz exponent of a grid function f_j (e.g. the density and pressure). The Lipschitz exponent at a point x is defined as the largest γ satisfying

$$\sup_{h\neq 0}\frac{|f(x+h)-f(x)|}{h^{\gamma}}\leqslant C, \tag{28}$$

and this gives information about the regularity of the function f, where small γ means poor regularity. For example, a continuous function $f(x)$ has a Lipschitz exponent $\gamma > 0$. A bounded discontinuity (shock) has $\gamma = 0$, and a Dirac function (local oscillation) has $\gamma = -1$. Large values of γ can be used in turbulent flow so that large vortices or vortex sheets can be detected. For a C^1 wavelet function $\psi(x)$ with compact support γ can be estimated from the wavelet coefficients, w_{mj}, defined as

$$w_{mj}=\langle f,\psi_{mj}\rangle=\int f(x)\psi_{mj}(x)dx, \tag{29}$$

where

$$\psi_{mj}=2^{m}\psi\left(\frac{x-j}{2^{m}}\right) \tag{30}$$

is the wavelet function ψ_{mj} on scale m located at the point j in space. In practical computations there is a smallest scale determined by the grid size. To estimate the Lipschitz exponent at $j = j_0$, we evaluate w_{mj} on the smallest scale, m_0, and a few coarser scales, $m_0 + 1$, $m_0 + 2$, and perform a least squares fit to the line [27]

$$\max_{j\ \text{near}\ j_0}\log_2|w_{mj}|=m\gamma+c. \tag{31}$$

For example, the Lipschitz exponent with a value near zero, -1 or wavelets with high-order vanishing moments indicate of the flow with a discontinuity, spurious local high frequency oscillations or large vortices. The flow sensor $(s^N)^l_{j+1/2}=1$ (or 0) is to turn on (or off) the shock-capturing dissipation at the "trouble areas". For more details about the wavelet and the flow sensor, we refer the readers to [27,38].

4. Description of well-balanced methods and construction of high-order well-balanced filter scheme

A well-balanced scheme is a scheme that exactly preserves specific steady-state solutions of the governing equations. In the previous work [29], certain linear schemes (including those used in this paper as the base schemes for the filter schemes), WENO-Roe schemes, the Harten–Yee TVD scheme, and Predictor–Corrector TVD schemes (with zero entropy correction) were proven theoretically and numerically to be well-balanced schemes for the non-equilibrium flow Eq. (2) with zero-velocity steady states. We refer to [29] for more details and will not repeat the descriptions of these well-balanced schemes here. A well-balanced finite difference WENO-LF scheme was also constructed with a limiter λ in the Lax–Friedrichs flux splitting

$$f^{\pm}(u)=\frac{1}{2}(f(u)\pm\alpha\lambda u). \tag{32}$$

λ is close to 0 or 1 according to whether the solution is in steady state or away from steady state. λ is constructed by

$$\begin{aligned}\lambda:\max&\left(\min\left(1,\frac{(|r_1(U_{i+1},x_{i+1})-r_1(U_i,x_i)|+|r_1(U_{i-1},x_{i-1})-r_1(U_i,x_i)|)^2}{|r_1(U_{i+1},x_{i+1})-r_1(U_i,x_i)|^2+|r_1(U_{i-1},x_{i-1})-r_1(U_i,x_i)|^2+\varepsilon}\right),\right.\\ &\left.\min\left(1,\frac{(|r_2(U_{i+1},x_{i+1})-r_2(U_i,x_i)|+|r_2(U_{i-1},x_{i-1})-r_2(U_i,x_i)|)^2}{|r_2(U_{i+1},x_{i+1})-r_2(U_i,x_i)|^2+|r_2(U_{i-1},x_{i-1})-r_2(U_i,x_i)|^2+\varepsilon}\right),\dots\right),\end{aligned} \tag{33}$$

where ε is an infinitesimal quantity to avoid zero in the denominator and $\varepsilon = 10^{-6}$ is used in the computations. The limiter does not affect the high-order accuracy of the scheme in smooth region for general solutions of Eq. (2). In the specific steady state, since all the r_i are constants, λ becomes zero and then the scheme maintains the exact solutions for such steady state. The functions r_i in the limiter (33) are used to distinguish between steady and unsteady states, we again refer to [29] for the details of these functions and will not give their expressions here.

The construction of high-order well-balanced filter schemes is straightforward. The first step is to choose any well-balanced low-dissipative scheme, e.g. a central scheme (CENx), or a predictor corrector scheme (PCx) (here x denotes the order of accuracy of the scheme, and will be 2, 4, 6, or 8) as base scheme. The second step is to choose a well-balanced filter, such as the dissipative portion of the TVD scheme or the high-order well-balanced WENO scheme. In fact, it was proved in [29] that at the zero-velocity steady-state solution, $R_{j+1/2}\overline{H}_{j+1/2}$ in Eq. (26) is zero and thus can be used as the filter part for a well-balanced filter scheme.

Here, we would like to remark that these constructed filter schemes are well-balanced, except at the interface between the filtered and non-filtered regions. Because in the interface of these two regions, the numerical fluxes get information from different schemes (base scheme part and filter part), the schemes will not be well-balanced at those interface cells. This is not a serious concern, since the interface is only a small portion of the whole computational domain. Also, since the filter is turned on only at the shock region, the transition region of the shock is usually far away from the considered zero-velocity steady state. Thus, there is no need to require the schemes to be well-balanced at the interfaces.

The linear dissipation part $d(\Delta x)^7(D_+D_-)^4U_j$ in the base scheme (24) cannot preserve the steady-state solutions. Similar to the Lax–Friedrichs flux, since there are no assumptions on the density functions, the dissipation $d(\Delta x)^7(D_+D_-)^4U_j$ may produce non-zero values in the steady states. Here, the same idea of constructing well-balanced WENO-LF schemes is applied, i.e. multiplying a limiter λ (33) to the linear dissipation part to turn off the linear dissipation in the steady-state area. Since the linear dissipation is only needed for stability concern before reaching steady state, numerical tests show that turning it off by the limiter λ does not affect the stability of the solution. With the limiter λ, the filter schemes will have no linear dissipation in the steady state and thus will maintain the exact steady-state solutions.

In this paper the considered well-balanced filter schemes are low-order central filter schemes with TVD filter (CEN2TVDfi and CEN4TVDfi), and high-order central filter schemes with balanced WENO filter (CEN6WENO5fi and CEN8WENO7fi). Similar considered PC filter schemes are PC2TVDfi, PC4TVDfi, PC6WENO5fi and PC8WENO7fi. For the same order PC and central filter schemes, the accuracies are similar. Comparing to central filter schemes, PC filter schemes allow a larger CFL number for time integration. However, the PC filter schemes only allow first- and second-order time discretizations. The central filter schemes allow a wider class of time discretizations.

5. Reaction model and test cases

In this section, the gas model comprised of five species N_2, O_2, NO, N, and O is described. Then, different numerical tests of the considered high-order well-balanced filter schemes for one- and two-dimensional reacting flows are performed. The first example is to numerically verify that the constructed filter schemes are well-balanced by time marching on a non-trivial steady state. In this test the well-balanced filter schemes will show round-off numerical errors for a specific steady-state solution. The second example is a small perturbation over the steady state. We can observe the well-balanced filter schemes showing their advantage in resolving the perturbations in very coarse meshes. For these problems, we use an explicit second-order Runge–Kutta method in time. The CFL number is 0.2–0.5 according to the order of the schemes.

For 1D numerical tests, we show three additional examples involving shocks. The first one is a stationary contact discontinuity problem, where the left and right states of the discontinuity are both in equilibrium. We will show that if there are small perturbations on the two sides of the discontinuity, the well-balanced schemes can capture them very accurately. The second shock example is a 1D turbulence/shock interaction problem where only the right state of the shock is in equilibrium. If there are small perturbations on the right of the shock, the well-balanced schemes will well resolve them, then when the shock passes through those perturbations, well-balanced schemes will have more accurate results than the non-well-balanced scheme on the left of the shock. The third example is a shock tube problem to test the shock-capturing capability of the considered schemes. This numerical test case is to demonstrate that well-balanced schemes will not destroy the non-oscillatory shock resolution away from the steady state. For those problems, a second-order implicit–explicit Runge–Kutta method in time is used (see the Appendix). The CFL number varies on the stiffness of the problems.

5.1. Reaction model

The air mixture is comprised of five species, N_2, O_2, NO, N, and O, with elemental fractions 79% for nitrogen and 21% for oxygen. The spectroscopic constants used in the computation of the species thermodynamic properties (θ_s^V, $\theta_{s,n}^E$, θ_s^R, g_s^E in Section 2) and the formation enthalpies are obtained from Gurvich et al. [8]. The chemical mechanism is comprised of three dissociation recombination reactions for molecules

$$N_2 + M \rightleftharpoons 2N + M \quad (\text{see } [22]) \tag{34}$$

$$O_2 + M \rightleftharpoons 2O + M \quad (\text{see } [22]) \tag{35}$$

$$NO + M \rightleftharpoons N + O + M \quad (\text{see } [21]) \tag{36}$$

where M is a catalytic particle (any of the species N_2, O_2, NO, N, and O), and two Zeldovich reactions for NO formation

$$N_2 + O \rightleftharpoons NO + N \quad (\text{see } [2]) \tag{37}$$

$$O_2 + N \rightleftharpoons NO + O \quad (\text{see } [3]) \tag{38}$$

5.2. One dimensional numerical results

5.2.1. Well-balanced test

The purpose of the first test problem is to numerically verify the well-balanced property of the proposed filter schemes. The special zero-velocity stationary case with

$$T = 1000 \times (1 + 0.2\sin(\pi x))K, \quad p = 10^5\ \mathrm{N/m^2}, \quad u = 0\ \mathrm{m/s}, \tag{39}$$

is considered. The initial composition is based on the local thermodynamic equilibrium (LTE) assumption. Given Eq. (39) and the source term $S(U) = 0$, each species is uniquely determined.

Eq. (39) is chosen as the initial condition which is also the exact steady-state solution, and the results are obtained by time-accurate time marching on the steady state. The computational domain is $[-1,1]$. The L^1 relative errors of temperature at $t = 0.01$ (about 1000 time steps for $N = 100$ grid points) are listed in Table 1. The L^1 relative error is measured to be the difference between the exact solution Eq. (39) and the numerical solution divided by the L^1 norm of the exact solution. We emphasize again that the exact steady-state solution is *not* a constant or a polynomial function, making it non-trivial for the well balanced schemes to achieve round-off level errors on all grids.

Table 1 shows that the considered high-order central filter schemes and PC filter schemes are well-balanced because they produce errors at the level of machine round-off errors in double precision. For comparison, the results by fifth-order WENO schemes are also listed in Table 2. The WENO-Roe scheme and balanced WENO-LF scheme produce round-off errors. However, the WENO-LF without the limiter lambda in (33) is not well-balanced and shows truncation errors in the computation.

An interesting test case is to show the comparison of the well-balanced schemes and the non-well-balanced schemes on the convergence history of time marching to steady states. For this purpose, initially we add a perturbation $\epsilon = 0.1 \times \sin(\pi x)$ to the momentum component of the steady-state solution (39). Fig. 1 plots the L^1 error of momentum versus the computational time of the balanced WENO-LF scheme and the regular WENO-LF scheme. The well-balanced scheme can go down till machine round-off error, indicating that it reaches the steady state of the PDE with time marching. However the non-well-balanced scheme with 50 grid points produces an error at the level of 10^{-3}, which is the truncation error for this scheme at this mesh size. The example shows the advantage of using well-balanced scheme time marching to steady states.

5.2.2. Small perturbation

The following test problem will demonstrate the advantages of well-balanced schemes through the problem of a small perturbation over a stationary state.

The same stationary solution, Eq. (39), is considered. A small perturbation $\epsilon = 10^{-3} \times \sin(\pi x)$ is added to the initial condition for velocity, i.e.

$$u' = u + \epsilon \tag{40}$$

Table 1
L^1 relative errors for temperature by central/PC filter schemes at $t = 0.01$.

N	Error CEN2TVDfi	Error CEN4TVDfi	Error CEN6WENO5fi	Error CEN8WENO7fi
50	3.84E−11	3.84E−11	3.79E−11	3.67E−11
100	3.79E−11	3.79E−11	3.68E−11	3.62E−11
	PC2TVDfi	PC4TVDfi	PC6WENO5fi	PC8WENO7fi
50	3.83E−11	3.76E−11	3.69E−11	3.63E−11
100	3.88E−11	3.85E−11	3.81E−11	3.78E−11

Table 2
L^1 relative errors for temperature by fifth-order WENO schemes at $t = 0.01$.

N	Error WENO-Roe	Error WENO-LF	Error balanced WENO-LF
50	3.92E−11	2.31E−05	3.90E−11
100	3.92E−11	8.29E−07	3.92E−11

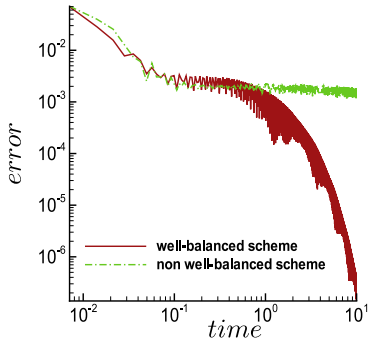

Fig. 1. Convergence history towards the steady state by the well-balanced and non-well-balanced WENO schemes with 50 points.

at $t = 0$. The other quantities are kept unperturbed. Fig. 2 shows the velocities by central and PC filter schemes of orders 2, 4, 6 and 8 at $t = 0.1$. The reference results are computed by fifth-order WENO-Roe with 1200 points.

The results show that all the considered high-order well-balanced filter schemes can capture the small perturbation well in a very coarse mesh. Especially for the schemes with order higher than 2, only 50 points are used. However, the non-well-balanced schemes behave in a very oscillatory fashion, such as the regular WENO-LF with 200 points (Fig. 3). They can only resolve the solution when the mesh is refined enough such that the truncation error of the scheme is much smaller than the perturbation.

5.2.3. 1D stationary contact discontinuity problem

The third example is a 1D stationary contact discontinuity problem on the domain $[-5,5]$. A stationary contact discontinuity is located at $x = 0$. The flow contains zero velocity and constant pressure 20 N/m^2 everywhere. The temperature has an initial condition

$$T = \begin{cases} 500 \times (1 + 0.1\sin(2\pi x)), & x < 0, \\ 300 \times (1 + 0.1\sin(2\pi x)), & x > 0. \end{cases} \tag{41}$$

The densities for each species can be solved by LTE condition. We add a small perturbation of the velocity over the whole domain

$$u' = u + 0.05 \times \sin(\pi x). \tag{42}$$

The computation stops at time $t = 0.01$. We remark that the solutions were computed on a larger domain $[-6,6]$ but truncated on $[-5,5]$ for not considering the effects by the boundary condition. Figs. 4 and 5 show the densities, temperatures, velocities and pressures by the balanced WENO-LF scheme and the regular WENO-LF scheme with 100 cells. The reference solution is computed by the WENO-Roe scheme with 1200 cells. From Fig. 4 we can see that the balanced WENO-LF produces a more accurate result than the regular WENO-LF scheme. The regular WENO-LF scheme has a discrepancy from the reference solution on the waves and it cannot capture the small wave close to the shock. Unlike the density and temperature, the velocity and pressure are constant at the initial time. Thus it is more clear to see the difference between the balanced WENO-LF and the regular WENO-LF on the velocity and pressure results. From Fig. 5, we can see the results by the balanced WENO-LF are indistinguishable from the reference solution. However, the regular WENO-LF produces large oscillations due to the truncation errors.

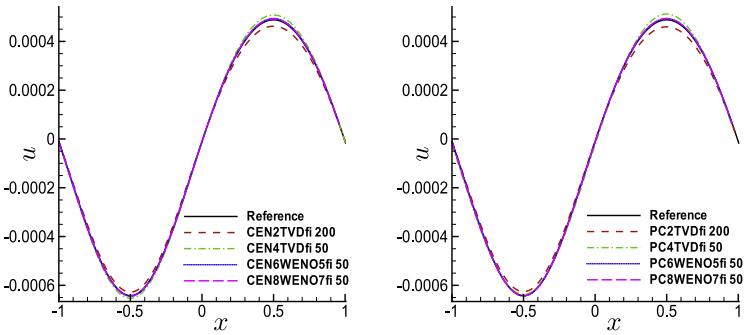

Fig. 2. Small perturbation of velocity results by filter schemes: $\epsilon = 10^{-3} \times \sin(\pi x)$. Solid lines are the reference 1200 point solution. Left: central filter schemes and right: PC filter schemes.

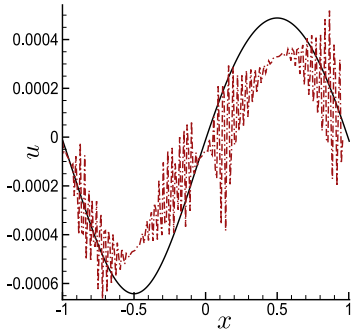

Fig. 3. Small perturbation of velocity results by WENO-LF scheme: $\epsilon = 10^{-3} \times \sin(\pi x)$. WENO-LF 200 points: dash-dot and reference 1200 points: solid.

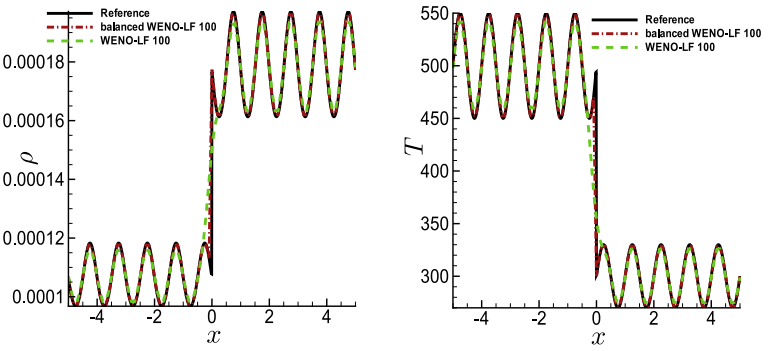

Fig. 4. 1D stationary contact discontinuity problem by WENO-LF schemes. Left: density of O_2 and right: temperature.

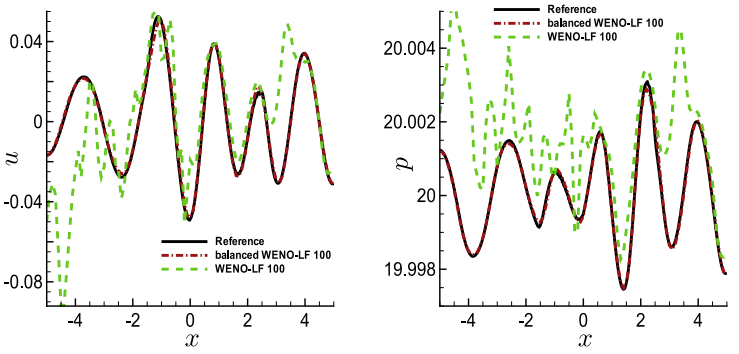

Fig. 5. 1D stationary contact discontinuity problem by WENO-LF schemes. Left: velocity and right: pressure.

Figs. 6 and 7 show the results by the central filter schemes. The considered central filter schemes here are CEN2TVDfi and CEN4TVDfi with 200 cells, and CEN6WENO5fi and CEN8WENO7fi with 100 cells. Similar for PC filter schemes, the results by PC2TVDfi, PC4TVDfi with 200 cells and PC6WENO5fi and PC8WENO7fi with 100 cells are shown in Figs. 8 and 9. All the well-balanced central/PC filter schemes can capture the small perturbations very well.

5.2.4. 1D shock/turbulence interaction problem

The fourth example is a 1D shock/turbulence interaction problem (also referred to as the Shu–Osher problem [25]) for reacting flows on the domain $[-5,5]$. Initially a shock is located at $x = -4$. The shock is moving at the speed 500m/s to the right. The right state of the flow consists two parts, the first part is a constant equilibrium state from -4 to 1 and the second part is an oscillatory equilibrium state from 1 to 5 with sine waves in densities and temperature.

The conditions are given by

$$(T_R, p_R, u_R) = \begin{cases} (500, 20, 0), & x \in [-4, 1], \\ (500 \times (1 + 0.1\sin(2\pi x)), 20, 0), & x \in [1, 5]. \end{cases} \tag{43}$$

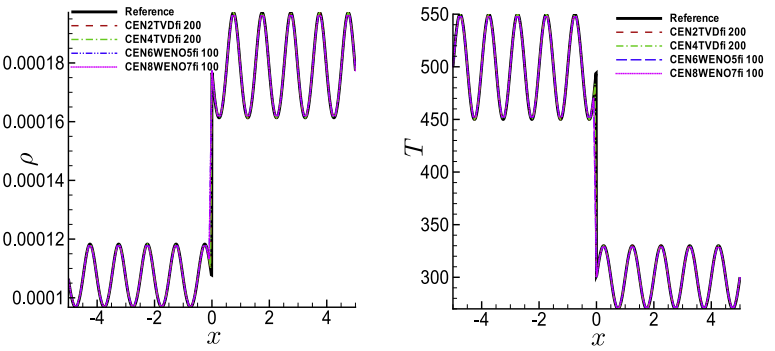

Fig. 6. 1D stationary contact discontinuity problem by central filter schemes. Left: density of O_2 and right: temperature.

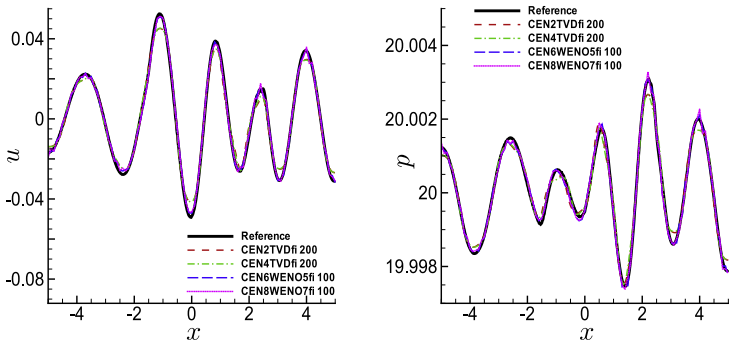

Fig. 7. 1D stationary contact discontinuity problem by central filter schemes. Left: velocity and right: pressure.

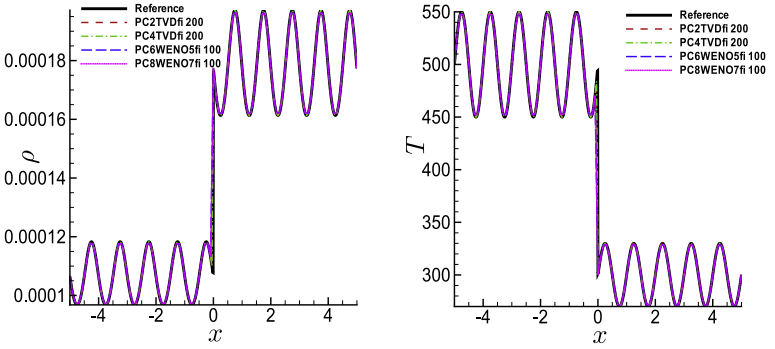

Fig. 8. 1D stationary contact discontinuity problem by PC filter schemes. Left: density of O_2 and right: temperature.

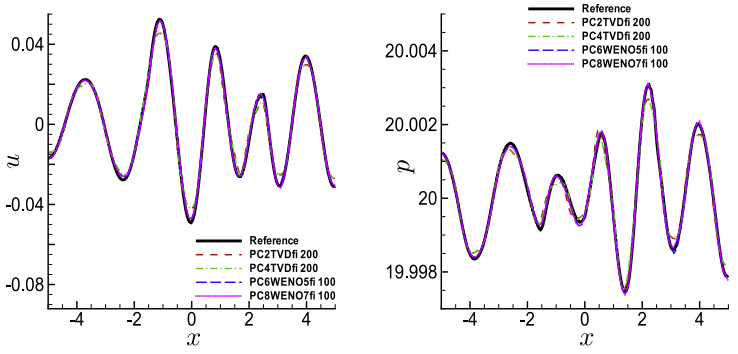

Fig. 9. 1D stationary contact discontinuity problem by PC filter schemes. Left: velocity and right: pressure.

Given the temperature and pressure, the densities for each species at the LTE state can be uniquely determined by the LTE condition. The left equilibrium state can be calculated according to the Rankine–Hugoniot jump condition.

Since the right state of the flow is a zero-velocity LTE state, the well-balanced schemes can resolve it with machine round-off errors. If we add a small perturbation of the velocity all over the right state

$$u' = u + 10^{-3} \times \sin(\pi x), \quad x \in [-4, 5], \tag{44}$$

the well-balanced schemes will be able to capture this small perturbation very well.

At time equal to 0.012 s, the shock moves to $x = 2$. The shock first passed through the small perturbation of the velocity and then passed through one sine wave (at the region $x \in [1,2]$).

The reference solution is computed by WENO-Roe with 2000 cells. Figs. 10 and 11 show the comparison of the regular fifth-order WENO-LF scheme and the balanced fifth-order WENO-LF scheme on velocity and pressure with 100 cells. From the global views of velocity and pressure (the left subplots of Figs. 10 and 11), we can hardly see any differences between these two schemes. However, zooming in the region $[-5,1]$, we can see that the balanced WENO-LF scheme can capture

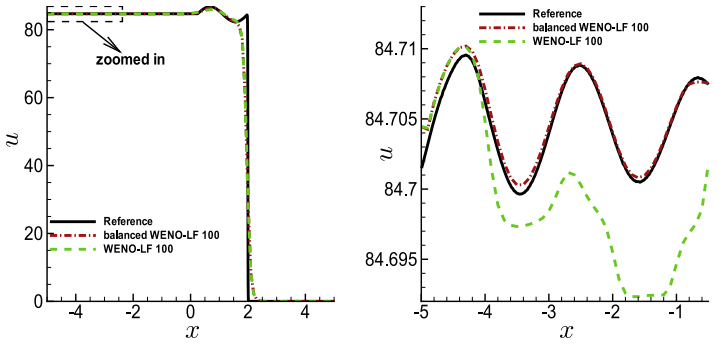

Fig. 10. 1D Shu–Osher problem of velocity results by WENO-LF schemes. Left: global and right: zoomed in.

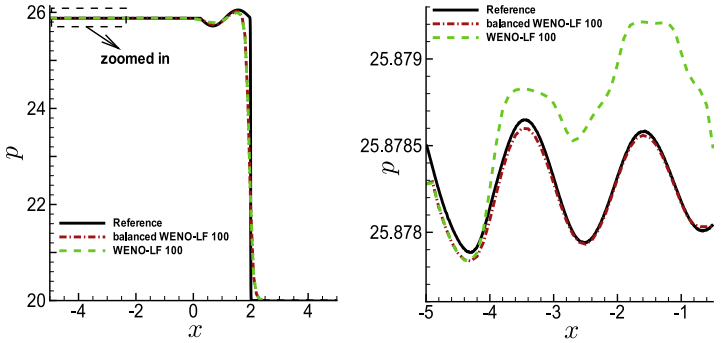

Fig. 11. 1D Shu–Osher problem of pressure results by WENO-LF schemes. Left: global and right: zoomed in.

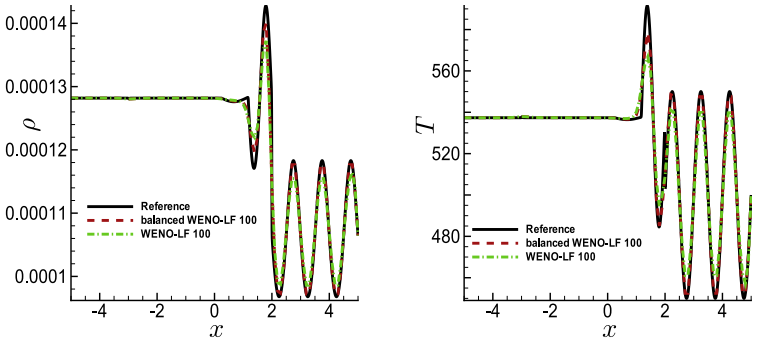

Fig. 12. 1D Shu–Osher problem by WENO-LF schemes. Left: density and right: temperature.

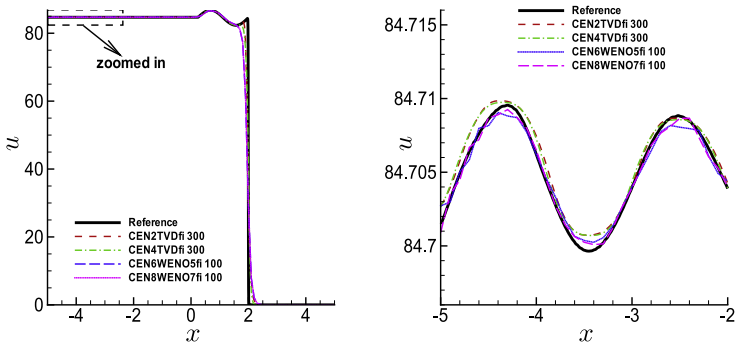

Fig. 13. 1D Shu–Osher problem of velocity results by central filter schemes. Left: global and right: zoomed in.

the small perturbation very well, whereas the regular WENO-LF scheme which is not well-balanced produces significantly larger errors (the right subplots of Figs. 10 and 11). The density and temperature results by the WENO-LF schemes are also shown in Fig. 12. We remark that the shock is located at $x = 2$ which is captured by the reference solution. However, the computed solutions by the considered schemes cannot resolve it very well due to the coarse meshes.

The results by central and PC filter schemes are shown in Figs. 13–18. The well-balanced schemes are proposed to have advantages for the region close to the steady state, so we only focus on the regions away from the shocks ($x \in [-5, -2]$). The considered central filter schemes here are CEN2TVDfi and CEN4TVDfi with 300 cells, and CEN6WENO5fi and CEN8WENO7fi with 100 cells. The considered PC filter schemes here are PC2TVDfi and PC4TVDfi with 300 cells, and PC6WENO5fi and PC8WENO7fi with 200 cells. Because for the moving shock problem, the filtered region is moving with the shock, and the switches between filtered and unfiltered will cause non-well-balancedness, the results of moving shock in this section are not as impressive as the results of the stationary contact discontinuity in Section 5.2.3 for such filtered schemes. We

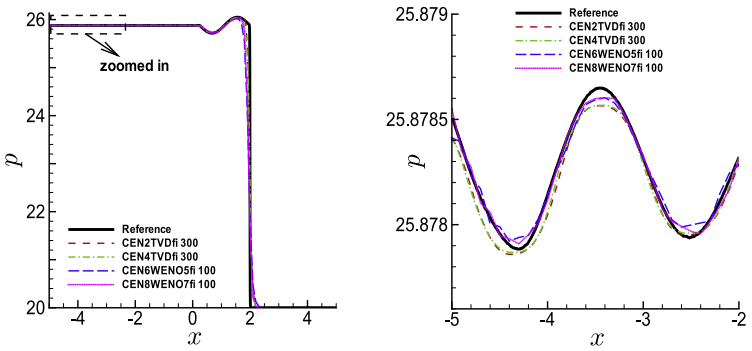

Fig. 14. 1D Shu–Osher problem of pressure results by central filter schemes. Left: global and right: zoomed in.

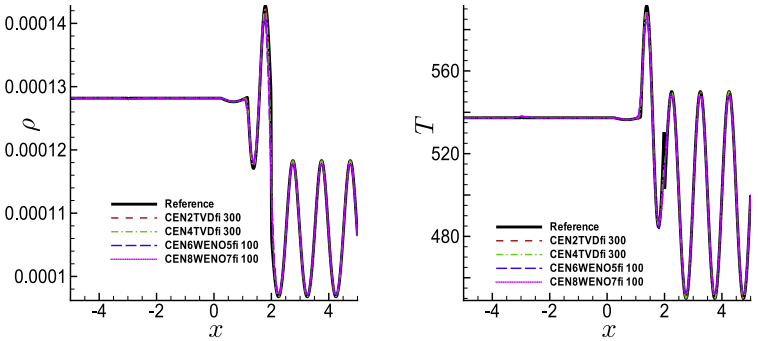

Fig. 15. 1D Shu–Osher problem by central filter schemes. Left: density and right: temperature.

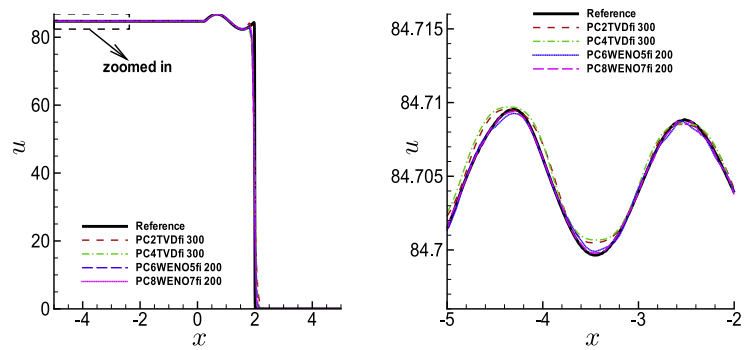

Fig. 16. 1D Shu–Osher problem of velocity results by PC filter schemes. Left: global and right: zoomed in.

use a more refined mesh for low-order schemes CEN2TVDfi, CEN4TVDfi, PC2TVDfi and PC4TVDfi. High-order schemes CEN6-WENO5fi and CEN8WENO7fi with 100 cells have underresolved solutions in the crest and trough of the waves. PC6WENO5fi and PC8WENO7fi with a more refined mesh 200 cells can resolve them better.

5.2.5. A shock tube problem

The last 1D example is a shock tube problem. A diaphragm is located at $x = 0$ which separates the right chamber from the left chamber. The right chamber has cold air with pressure $0.6 \times 10^5 \mathrm{N/m^2}$ and temperature 300 K. The gas in the left chamber has high pressure $6 \times 10^5\ \mathrm{N/m^2}$ and high temperature 3000 K. Both gases are in LTE condition. The computational domain is $[-5,5]$ in the lab frame.

The results are computed at $t = 0.001$. The solution is no longer in steady state. This example is to test the shock capturing ability of our well-balanced filter schemes. The numerical results of temperature, velocity and mass fraction of N_2 (from left to right) computed by CEN8WENO7fi and PC8WENO7fi are plotted in Figs. 19 and 20. As expected, the rarefaction wave, contact surface and shock appear in the temperature solution. Since the velocity is consistent through the contact surface, there

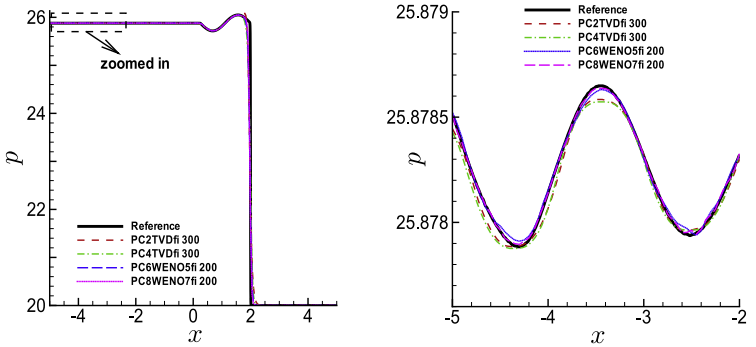

Fig. 17. 1D Shu–Osher problem of pressure results by PC filter schemes. Left: global and right: zoomed in.

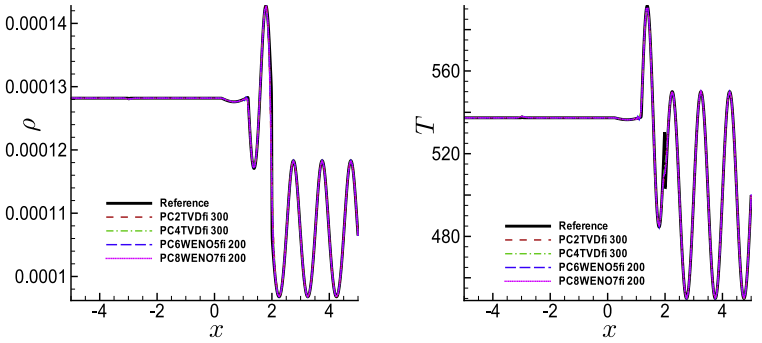

Fig. 18. 1D Shu–Osher problem by PC filter schemes. Left: density and right: temperature.

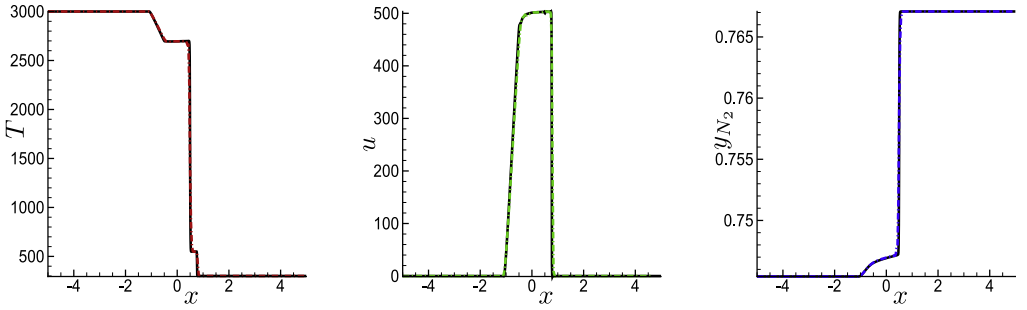

Fig. 19. Shock tube problem by CEN8WENO7fi. Left: temperature; middle: velocity and right: mass fraction of N_2 (CEN8WENO7fi with 300 points: dash-dot; Reference 1200 points: solid).

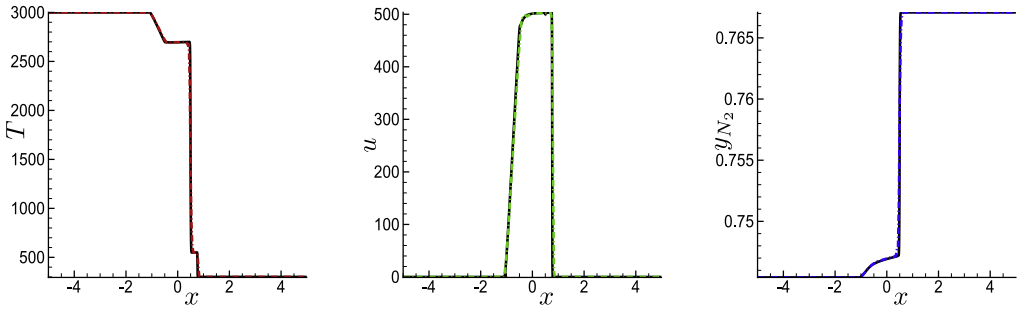

Fig. 20. Shock tube problem by PC8WENO7fi: Left: temperature; middle: velocity and right: mass fraction of N_2 (PC8WENO7fi with 300 points: dash-dot; Reference 1200 points: solid).

are only rarefaction wave and shock appearing in the velocity solution. Furthermore, mass is conserved during the shock. No shock appears in the mass solution. All the considered well-balanced filter schemes can capture the shocks sharply without oscillations.

5.3. Nozzle flow

The one-dimensional non-equilibrium nozzle flow takes the form

$$\begin{aligned}
&(\rho_i A)_t + (\rho_i u A)_x = b^i A, \quad i = 1, \ldots, n_s,\\
&(\rho u A)_t + \left((\rho u^2 + p)A\right)_x = pA'(x),\\
&(\rho e A)_t + ((\rho e + p)uA)_x = 0,
\end{aligned} \tag{45}$$

where $A = A(x)$ denotes the area of the cross section and b^i are the reacting terms in Eq. (3).

Different from Eq. (2), the nozzle flow has an additional source term on the momentum equation which needs special treatment for the schemes in order to be well-balanced. We perform similar tests as the last section. The first example is used to test whether the scheme can preserve the steady-state solution exactly. The second example is to show the capability of well-balanced schemes for the small perturbation problems.

5.3.1. Well-balanced test

Assuming the cross section function takes the form

$$A(x) = 1 + 0.2\sin(\pi x). \tag{46}$$

Consider the special steady state

$$T = 1000\ \text{K}, \quad p = 10^5\ \text{N/m}^2, \quad u = 0\ \text{m/s}, \tag{47}$$

with periodic boundary conditions. Eq. (47) is also the initial condition for the time marching on steady state. Notice that this additional source term needs to be treated by the same approximation method for the flux F in order to construct the well-balanced schemes; we refer to [29] for the details.

The L^1 relative errors for temperature by central/PC filter schemes at $t = 0.01$ is listed in Table 3. The central and PC filter schemes are well-balanced which produce round-off errors.

5.3.2. Small perturbation

Next, we add a small perturbation on the velocity component, i.e.

$$u' = u + \varepsilon, \tag{48}$$

with $\varepsilon = 0.001\sin(\pi x)$. We plot the comparison of the well-balanced schemes and the non-well-balanced schemes on the result of velocity at $t = 0.01$ in Fig. 21. The reference solution is computed by fifth-order WENO-Roe with 1000 points. The well-

Table 3
L^1 relative errors for temperature by central/PC filter schemes at $t = 0.01$.

N	Error CEN6WENO5fi	Error CEN8WENO7fi	Error PC6WENO5fi	Error PC8WENO7fi
50	3.29E−11	3.29E−11	3.29E−11	3.29E−11
100	3.29E−11	3.30E−11	3.29E−11	3.29E−11

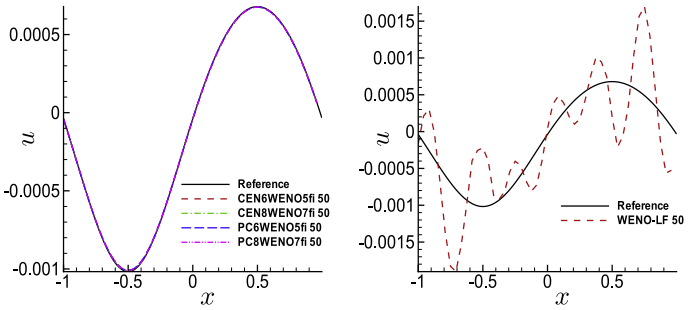

Fig. 21. Small perturbation in nozzle flow: Left: well-balanced schemes and right: non-well-balanced schemes.

balanced schemes such as central filter and PC filter schemes with 50 points can capture the small perturbation very well (left subplot of Fig. 21) whereas the non-well-balanced scheme such as WENO-LF has large oscillations in the coarse mesh (right subplot of Fig. 21).

5.4. 2D numerical results

As mentioned in the beginning, extending the well-balanced schemes to the zero-velocity steady state of 2D reacting flow is trivial because the reacting term does not depend explicitly on the spatial coordinates. In this section, similar well-balanced tests to 2D reacting flow will be performed.

5.4.1. 2D well-balanced test

Similar to the 1D case, the first example is to check that the proposed schemes maintain the 2D zero-velocity steady state exactly. The 2D special stationary case

$$T = 1000 \times (1 + 0.2\sin(\pi(x+y)))\ \mathrm{K}, \quad p = 10^5\ \mathrm{N/m^2}, \quad u = 0\ \mathrm{m/s}, \tag{49}$$

is considered. The computation is performed to $t = 0.01$ (about 2000 time steps for 100×100 grid points) on the domain $[-1,1]^2$. Table 4 shows the L^1 relative errors for the temperature T. We can clearly see that the L^1 relative errors are at the level of round-off errors, verifying the well-balancedness of the considered central filter and PC filter schemes for 2D reacting flow. For comparison, the results by fifth-order WENO schemes are also listed in Table 5. The WENO-Roe scheme and balanced WENO-LF scheme produce round-off errors. However, the regular WENO-LF, which is not well-balanced, shows truncation errors in the computation.

5.4.2. 2D small perturbation test

The second example is again a small perturbation test but on a 2D steady state. The same 2D steady-state solution Eq. (49) is considered. A small perturbation $\epsilon = 10^{-3} \times \sin(\pi(x+y))$ is added to the initial condition of velocity in the x direction, i.e.

$$u' = u + \epsilon \tag{50}$$

Table 4
L^1 relative errors for temperature by central/PC schemes at $t = 0.01$.

$N \times N$	Error CEN2TVDfi	Error CEN4TVDfi	Error CEN6WENO5fi	Error CEN8WENO7fi
50×50	4.14E−11	4.14E−11	4.21E−11	4.30E−11
100×100	4.04E−11	3.69E−11	3.73E−11	3.82E−11
	PC2TVDfi	PC4TVDfi	PC6WENO5fi	PC8WENO7fi
50×50	4.13E−11	4.20E−11	4.24E−11	4.29E−11
100×100	4.03E−11	4.07E−11	4.10E−11	4.13E−11

Table 5
L^1 relative errors for temperature by fifth-order WENO schemes at $t = 0.01$.

$N \times N$	Error WENO-Roe	Error WENO-LF	Error balanced WENO-LF
50×50	3.91E−11	4.59E−05	3.91E−11
100×100	3.92E−11	1.61E−06	3.92E−11

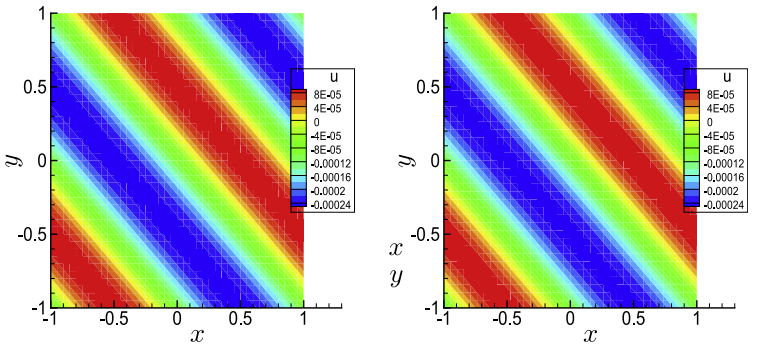

Fig. 22. 2D small perturbation of velocity results by central filter schemes: velocity u. Left: CEN6WENO5fi 40 × 40 points and right: CEN8WENO7fi 40 × 40 points.

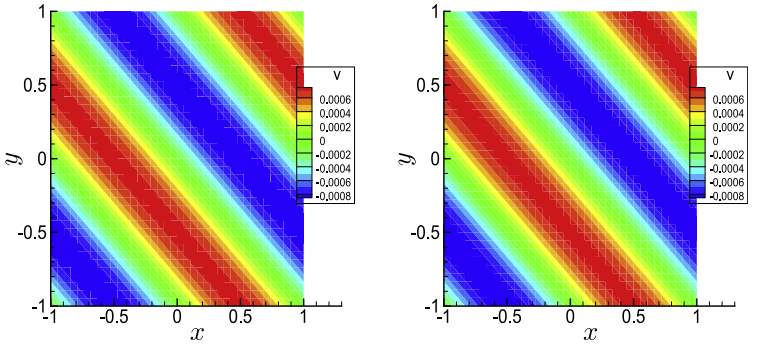

Fig. 23. 2D small perturbation of velocity results by PC filter schemes: velocity v. Left: PC6WENO5fi 40 × 40 points and right: PC8WENO7fi 40 × 40 points.

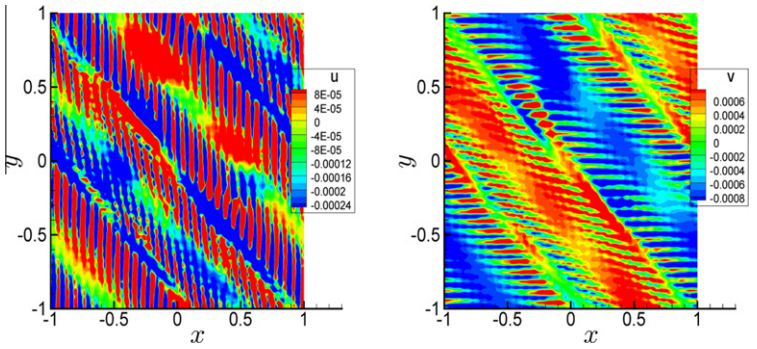

Fig. 24. 2D small perturbation of velocity results by WENO-LF schemes. Left: velocity u and right: velocity v. WENO-LF 100 × 100 points.

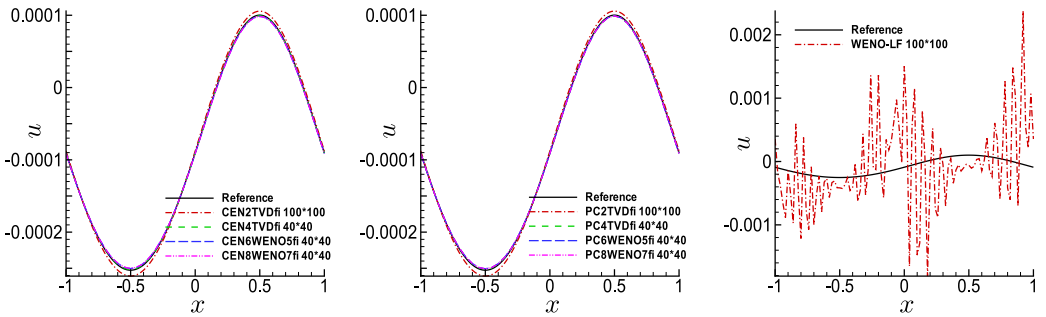

Fig. 25. Cross section of 2D velocity u at $y = 0$. Left: central filter schemes; middle: PC filter schemes and right: WENO-LF.

at $t = 0$. The other quantities are kept unperturbed. The reference solution is computed by WENO-Roe scheme with 200×200 points. Fig. 22 show the contours of velocity u by the sixth-order and eighth-order central WENO filter schemes at $t = 0.01$. For comparison, The results of velocity v are shown in Fig. 23 by sixth-order and eighth-order PC WENO filter schemes.

The contours of velocity u and v by regular WENO-LF are shown in Fig. 24. The 1D cross-section results by PC filter schemes, central filter schemes and WENO-LF are shown in Fig. 25 left, middle and right subplots separately. We can see that our well-balanced filter schemes can capture the small perturbation in a coarse mesh very well. However, the WENO-LF, which is not well balanced, produces large oscillations even in a mesh 100×100 (Fig. 24 and right subplots of Fig. 25).

6. Concluding remarks

In this paper the well-balanced approach is extended to the high-order filter schemes in solving five species reacting flow in one and two space dimensions. This is a generalization of our earlier work [29]. In addition, more general 1D and 2D reacting flow models and new examples of shock turbulence interactions are provided to demonstrate the advantage of well-balanced schemes. Numerical examples are given to demonstrate the well-balanced property, accuracy, good capturing of the small perturbation of the steady-state solutions, and the non-oscillatory shock resolution of the proposed well-balanced filter schemes. Because of the property of the zero-velocity steady-state solution of the reacting flow, the extension to any number of species and other reaction models is straightforward. Future research will consider the non-zero-velocity steady state and the advantages of well-balanced schemes to various steady-state problems.

Acknowledgments

The authors acknowledge the support of the DOE/SciDAC SAP Grant DE-AI02-06ER25796. Part of the work by the second author is performed under the NASA Fundamental Aeronautics Hypersonic Program. The work by the third author is performed under the auspices of the US Department of Energy by Lawrence Livermore National Laboratory under Contract DE-AC52-07NA27344, LLNL-JRNL-420355. The Mutation library for physico-chemical properties was developed under the European Office of Aerospace Research and Development of the US Air Force, Grant FA 8655–08-1–3070.

Appendix A. Spatial base schemes and time discretization

Samples of the high-order base schemes for F_x can be of the following types.

Central difference operators:

CEN4:

$$F_x \approx \frac{1}{12\Delta x}(-F_{j+2} + 8F_{j+1} - 8F_{j-1} + F_{j-2}), \tag{51}$$

CEN6:

$$F_x \approx \frac{1}{60\Delta x}(F_{j+3} - 9F_{j+2} + 45F_{j+1} - 45F_{j-1} + 9F_{j-2} - F_{j-3}). \tag{52}$$

Compact central difference operators [10,4,14]). Here

$$F_x \approx \frac{1}{\Delta x}(A_x^{-1}B_xF)_j, \tag{53}$$

where for a fourth-order approximation

$$\begin{aligned}(A_xF)_j &= \frac{1}{6}(F_{j+1} + 4F_j + F_{j-1}),\\ (B_xF)_j &= \frac{1}{2}(F_{j+1} - F_{j-1}),\end{aligned} \tag{54}$$

and a sixth-order approximation

$$\begin{aligned}(A_xF)_j &= \frac{1}{5}(F_{j+1} + 3F_j + F_{j-1}),\\ (B_xF)_j &= \frac{1}{60}(F_{j+2} + 28F_{j+1} - 28F_{j-1} - F_{j-2}).\end{aligned} \tag{55}$$

Predictor–corrector difference operators:

PC4:

$$D_pF_j = \frac{1}{6\Delta x}(7F_j - 8F_{j-1} + F_{j-2}),$$
$$D_cF_j = \frac{1}{6\Delta x}(-7F_j + 8F_{j+1} - F_{j+2}), \tag{56}$$

PC6:

$$D_pF_j = \frac{1}{30\Delta x}(37F_j - 45F_{j-1} + 9F_{j-2} - F_{j-3}),$$
$$D_cF_j = \frac{1}{30\Delta x}(-37F_j + 45F_{j+1} - 9F_{j+2} + F_{j+3}), \tag{57}$$

and PC8:

$$D_pF_j = \frac{1}{420\Delta x}(533F_j - 672F_{j-1} + 168F_{j-2} - 32F_{j-3} + 3F_{j-4}),$$
$$D_cF_j = \frac{1}{420\Delta x}(-533F_j + 672F_{j+1} - 168F_{j+2} + 32F_{j+3} - 3F_{j+4}), \tag{58}$$

where D_pF is the PC differencing operator approximating F_x at the first step (predictor step) and D_cF is the PC differencing operator at the second step (corrector step). New forms of the upwind-biased PC methods including compact formulations developed by Hixon and Turkel [11,12] are also applicable as spatial base schemes. Interested readers should refer to their paper for the various upwind-biased PC formulae. The choice of the time integrators for these types of PC methods is more limited. For example, if second-order time accuracy is desired, then (56)–(58) in conjunction with the appropriate second-order Runge–Kutta method are analogous to the familiar 2–4, 2–6 and 2–8 MacCormack schemes developed by Gottlieb and Turkel [6] and Bayliss et al. [1]. Here the first number refers to the order of accuracy for the time discretization and the second number refers to the order of accuracy or the spatial discretization. However, in this case one achieves the second-order time accuracy without dimensional splitting of the Strang type [28]. For higher than second-order time discretizations, only certain even stage Runge–Kutta methods are applicable. For compatible fourth-order Runge–Kutta time discretizations, see Hixon and Turkel for possible formulae. For example, the classical fourth-order Runge–Kutta is applicable provided one applies the predictor and the corrector step twice for the four stages, i.e. the predictor step for the first and third stages and the corrector step for the second and fourth stages.

For the considered 1D system with source term (2), the predictor–corrector scheme with 2nd-order implicit–explicit Runge–Kutta in time takes the form

$$U^{(1)} = U^n - \Delta t D_pF(t^n, U^n) + \Delta t S(t^n, U^n), \tag{59}$$
$$U^{n+1} = ((U^{(1)} + U^n) - \Delta t D_cF(t^{n+1}, U^{(1)}) + \Delta t S(t^{n+1}, U^{n+1}))/2, \tag{60}$$

The PC operators are modified at boundaries in a stable way by the summation-by-part (SBP) operators [19,18,35]. If D_b is the standard pth-order SBP for the centered difference operators, then the pth-order PC operators are modified as follows:

$$F_x \approx \begin{cases} D_pF_j, & j = n_b + 1, \ldots, N \\ (2D_b - D_c)F_j, & j = 1, \ldots, n_b \end{cases} \tag{61}$$

at the predictor step and

$$F_x \approx \begin{cases} D_cF_j, & j = 1, \ldots, N - n_b \\ (2D_b - D_p)F_j, & j = N - n_b + 1, \ldots, N \end{cases} \tag{62}$$

at the corrector step, where N is the number of grid points and n_b is the number of points that need boundary modified difference operators.

References

[1] A. Bayliss, P. Parikh, L. Maestrello, E. Turkel, A fourth-order scheme for the unsteady compressible Navier Stokes equations, in: AIAA Fluid Dynamics and Plasmadynamics and Lasers Conference, 18th, Cincinnati, OH, July 16–18, 1985.
[2] D. Bose, G.V. Candler, Thermal rate constants of the $N_2 + O \rightarrow NO + N$ reaction using ab initio $^3A''$ and $^3A'$ potential energy surfaces, J. Chem. Phys. 104 (1996) 2825–2833.
[3] D. Bose, G.V. Candler, Thermal rate constants of the $O_2 + N \rightarrow NO + O$ reaction based on the $^2A'$ and $^4A'$ potential-energy surfaces, J. Chem. Phys. 107 (1997) 6136–6145.
[4] M. Ciment, H. Leventhal, Higher order compact implicit schemes for the wave equation, Math. Comput. 29 (1975) 985–994.
[5] L. Gosse, A well-balanced flux-vector splitting scheme designed for hyperbolic systems of conservation laws with source terms, Comput. Math. Appl. 39 (2000) 135–159.
[6] D. Gottlieb, E. Turkel, Dissipative twofour methods for time dependent problems, Math. Comput. 30 (1976) 703–723.
[7] J.M. Greenberg, A.Y. Leroux, A well-balanced scheme for the numerical processing of source terms in hyperbolic equations, SIAM J. Numer. Anal. 33 (1996) 1–16.
[8] L.V. Gurvich, I.V. Veits, C.B. Alcock, Thermodynamic properties of individual substances, O, H/D,T/, F, Cl, Br, I, He, Ne, Ar, Kr, Xe, Rn, S, N, P, and their compounds, vol. 1, Part one: methods and computation, Part two: tables New York, Hemisphere Publishing Corp., 1989.

[9] A. Harten, The artificial compression method for computation of shocks and contact discontinuities: III. Self-adjusting hybrid schemes, Math. Comput. 32 (1978) 363–389.
[10] R.S. Hirsh, Higher order accurate difference solutions of fluid mechanics problems by a compact differencing technique, J. Comput. Phys. 19 (1975) 90–109.
[11] R. Hixon, E. Turkel, High-accuracy compact MacCormack-type schemes for computational aeroacoustics, in: AIAA-1998-365, Aerospace Sciences Meeting and Exhibit, 36th, Reno, NV, January 12–15, 1998.
[12] R. Hixon, E. Turkel, Compact implicit MacCormack-type schemes with high accuracy, J. Comput. Phys. 158 (2000) 51–70.
[13] G. Jiang, C.-W. Shu, Efficient implementation of weighted ENO schemes, J. Comput. Phys. 126 (1996) 202–228.
[14] S. Lele, Compact finite difference schemes with spectral-like resolution, J. Comput. Phys. 103 (1992) 16–42.
[15] R.J. LeVeque, Balancing source terms and flux gradients in high-resolution Godunov methods: the quasi-steady wave-propagation algorithm, J. Comput. Phys. 146 (1998) 346–365.
[16] R.J. LeVeque, H.C. Yee, A study of numerical methods for hyperbolic conservation laws with stiff source terms, J. Comput. Phys. 86 (1990) 187–210.
[17] T.E. Magin, L. Caillault, A. Bourdon, C.O. Laux, Nonequilibrium radiative heat flux modeling for the Huygens entry probe, J. Geophys. Res. 111 (2006) E07S12.
[18] J. Nordstrom, M.H. Carpenter, Boundary and interface conditions for high-order finite-difference schemes applied to the Euler and Navier–Stokes equations, J. Comput. Phys. 148 (1999) 621–645.
[19] P. Olsson, Summation by parts, projections and stability I, Math. Comput. 64 (1995) 1035–1065.
[20] M. Panesi, T.E. Magin, A. Bourdon, A. Bultel, O. Chazot, Analysis of the FIRE II flight experiment by means of a collisional radiative model, J. Thermophys. Heat Transfer 23 (2009) 236–248.
[21] C. Park, Review of chemical-kinetic problems of future NASA missions. I – Earth entries, J. Thermophys. Heat Transfer 7 (1993) 385–398.
[22] C. Park, R.L. Jaffe, H. Partridge, Chemical-kinetic parameters of hyperbolic Earth entry, J. Thermophys. Heat Transfer 15 (2001) 76–90.
[23] J. Qiu, B.C. Khoo, C.-W. Shu, A numerical study for the performance of the Runge–Kutta discontinuous Galerkin method based on different numerical fluxes, J. Comput. Phys. 212 (2006) 540–565.
[24] P.L. Roe, Approximate Riemann solvers, parameter vectors, and difference schemes, J. Comput. Phys. 43 (1981) 357–372.
[25] C.-W. Shu, S. Osher, Efficient implementation of essentially non-oscillatory shock capturing schemes, II, J. Comput. Phys. 83 (1989) 32–78.
[26] B. Sjögreen, H.C. Yee, Efficient low dissipative high order schemes for multiscale MHD flows, I: Basic theory, in: AIAA 2003-4118, Proceedings of the 16th AIAA/CFD Conference, 23–26 June 2003, Orlando, FL.
[27] B. Sjögreen, H.C. Yee, Multiresolution wavelet based adaptive numerical dissipation control for shock–turbulence computation, J. Sci. Comput. 20 (2004) 211–255.
[28] G. Strang, On the construction and comparison of difference schemes, SIAM J. Numer. Anal. 5 (1968) 506–517.
[29] W. Wang, C.-W. Shu, H.C. Yee, B. Sjögreen, High order well-balanced schemes and applications to non-equilibrium flow, J. Comput. Phys. 228 (2009) 5787–5802.
[30] Y. Xing, C.-W. Shu, High order finite difference WENO schemes with the exact conservation property for the shallow water equations, J. Comput. Phys. 208 (2005) 206–227.
[31] Y. Xing, C.-W. Shu, High order well-balanced finite difference WENO schemes for a class of hyperbolic systems with source terms, J. Sci. Comput. 27 (2006) 477–494.
[32] H.C. Yee, A class of high-resolution explicit and implicit shock-capturing methods, in: VKI Lecture Series 1989-04, March 6–10, 1989; NASA TM-101088, February 1989.
[33] H.C. Yee, N.D. Sandham, M.J. Djomehri, Low dissipative high order shock-capturing methods using characteristic-based filters, J. Comput. Phys. 150 (1999) 199–238.
[34] H.C. Yee, J.L. Shinn, Semi-implicit and fully implicit shock-capturing methods for nonequilibrium flows, AIAA J. 225 (1989) 910–934.
[35] H.C. Yee, B. Sjögreen, Designing adaptive low dissipative high order schemes for long-time integrations, in: D. Drikakis, B. Geurts (Eds.), Turbulent Flow Computation, Springer, October 2001.
[36] H.C. Yee, B. Sjögreen, Efficient low dissipative high order scheme for multiscale MHD flows, II: Minimization of Div(B) numerical error, J. Sci. Comput. 29 (2006) 115–164.
[37] H.C. Yee, B. Sjögreen, Nonlinear filtering and limiting in high order methods for ideal and non-ideal MHD, J. Sci. Comput. 27 (2006) 507–521.
[38] H.C. Yee, B. Sjögreen, Development of low dissipative high order filter schemes for multiscale Navier–Stokes/MHD systems, J. Comput. Phys. 68 (2007) 151–179.
[39] H.C. Yee, M. Vinokur, M.J. Djomehri, Entropy splitting and numerical dissipation, J. Comput. Phys. 162 (2000) 33–81.